CrossMark

J. Fluid Mech. (2017), *vol.* 819, *pp.* 1–20. © Cambridge University Press 2017
doi:10.1017/jfm.2017.140

Growth dynamics of turbulent spots in plane Couette flow

Marie Couliou[1] **and Romain Monchaux**[1,†]

[1]IMSIA, ENSTA ParisTech, CNRS, CEA, EDF, Université Paris-Saclay, 828 Boulevard des Maréchaux, 91762 Palaiseau CEDEX, France

(Received 18 February 2016; revised 9 February 2017; accepted 2 March 2017; first published online 18 April 2017)

We experimentally and numerically investigate the temporal aspects of turbulent spots spreading in a plane Couette flow for transitional Reynolds numbers between 300 and 450. Spot growth rate, spot advection rate and large-scale flow intensity are measured as a function of time and Reynolds number. All these quantities show similar dynamics clarifying the role played by large-scale flows in the advection of the turbulent spot. The contributions of each possible growth mechanism, that is, growth induced by large-scale advection or growth by destabilization, are discussed for the different stages of the spot growth. A scenario that gathers all these elements is providing a better understanding of the growth dynamics of turbulent spots in plane Couette flow that should possibly apply to other extended shear flows.

Key words: instability, transition to turbulence

1. Introduction

Transition to turbulence in wall-bounded shear flows often occurs through subcritical scenarios when their natural control parameter, the Reynolds number (Re), is increased. This is the case for plane Couette flow (PCF), Hagen–Poiseuille flow, Taylor–Couette flow (when the outer cylinder is rotating) and plane Poiseuille flow. In all these cases, the laminar profile is linearly stable for $Re < Re_c$ but it is actually observed to be nonlinearly destabilized by finite-amplitude perturbations above $Re_g < Re_c$. Below this threshold, Re_g, any perturbation brought to the laminar profile eventually vanishes. Above, the flow is highly sensitive to the nature and intensity of the perturbation. The ultimately observed state results from the competition between coexisting turbulent and laminar areas. When Re is larger than $Re_t > Re_g$, this final state consists of homogeneous featureless turbulence, while for $Re_g < Re < Re_t$, it involves both laminar and turbulent areas. This mixed state can be unpredictably evolving or steady and organized – as in the turbulent spiral formerly observed by Coles (1965) and Van Atta (1966) in Taylor–Couette flow and later characterized at a much larger aspect ratio by Prigent *et al.* (2002). In both cases, the laminar–turbulent interfaces are found to be oblique, a so far unexplained feature shared by all such patterns now observed in all the extended 'subcritical' flows cited above – see Barkley & Tuckerman (2005), Prigent & Dauchot (2005) and Duguet, Schlatter & Henningson

† Email address for correspondence: monchaux@ensta.fr

https://doi.org/10.1017/jfm.2017.140 Published online by Cambridge University Press

(2010) for plane Couette flow, and Hashimoto *et al.* (2009) and Tuckerman *et al.* (2014) for plane Poiseuille flow. These patterns are even observed in Waleffe flow, a shear flow without walls, as recently proven by Chantry, Tuckerman & Barkley (2016).

More basically, the simple development of turbulence within a formerly laminar state is far from being fully understood. From the early observations by Emmons (1951) in boundary layers, it obviously appears that localized perturbations trigger the growth of turbulent spots that consist of simply connected turbulent regions immersed in an otherwise laminar flow and bounded by fronts that move in order to expand the turbulent area provided Re is large enough. Turbulence in these kinds of transitional flows consists of long streamwise velocity streaks associated with counter-rotating vortices that are stacked together along the spanwise direction. As the wavelength of the streaky pattern is narrowly distributed around a given value λ_s, the spanwise growth of a turbulent spot corresponds to the nucleation of new streaks. The mechanisms at work to achieve this expansion have not yet all been revealed in spite of many experimental and numerical studies. Shedding light on the growth process of turbulent spots can also be a key point in understanding the formation and sustainment of organized patterns. In the case of plane Couette flow, for which no mean advection is present, turbulent spot growth can be split into two phases: in the first stage of their development, they grow in a more or less symmetric fashion, leading to diamond-like shape as seen in figure 1; and then, when their spatial extent is large enough, they start to become distorted, and tend to form oblique branches. As first evidenced numerically in the pioneering work by Lundbladh & Johansson (1991), the spot remains centro-symmetric all along the first phase. The flow and pattern symmetries are detailed in an extensive review (Barkley & Tuckerman 2007). Figure 1 gives an illustration of the growth of such a spot in our experiment around a localized perturbation. The spot is indeed elliptic, the principal axis along the streamwise direction being longer than that along the spanwise direction. As time passes, both principal axes tend to have the same length and the spot takes the form of a more or less regular diamond whose sides form an angle with respect to the streamwise direction. This angle is prefiguring the organized pattern orientation. This dynamic results from growth rates that are significantly larger in the spanwise than in the streamwise direction, as shown successively by the two experimental works by Tillmark & Alfredsson (1992) and by Dauchot & Daviaud (1995) confirming the numerical investigation by Lundbladh & Johansson (1991). These researchers focused on global growth rates along both relevant directions and found in first approximation that they were time-independent but increasing functions of the Reynolds number, as can be seen in figure 2 which gathers their time-average results of spanwise growth rate as a function of Re.

The second phase is illustrated in figure 1 at times larger than 400. Specific studies of this second phase are scarce. In very large domains, Duguet *et al.* (2010) nevertheless present the typical evolution of a diamond-shaped spot turning progressively into a turbulent pattern made of several adjacent bands with various orientations that are similar to the more steady patterns described above (see in particular their figures 2 and 4). In domains of moderate extension (say, when the spanwise direction is 40 times the distance between the walls), this second phase starts when the spot size becomes sizable with the domain spanwise extension and consists mostly of a reorganization of the turbulent area into an inclined pattern. In the following we will focus on the first phase.

Understanding the mechanisms responsible for the spot growth requires taking into account all the features of the spot during this first phase. From the numerical

https://doi.org/10.1017/jfm.2017.140 Published online by Cambridge University Press

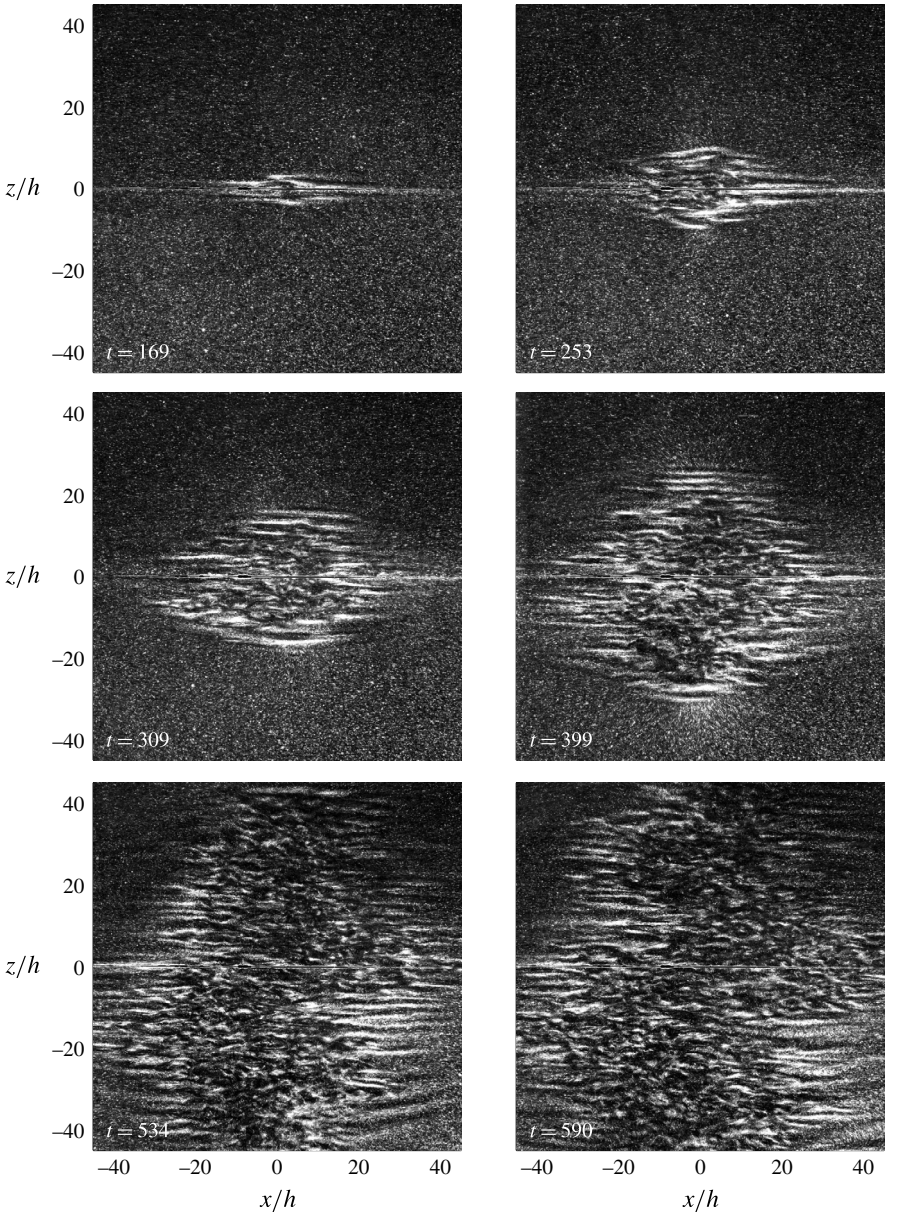


FIGURE 1. Snapshots of a spot growing around a bead during a step experiment (sudden increase at $t = 0$ of Re from 0 to 403). Times are given in units of h/U. The first phase lasts till $t \simeq 400h/U$ when the reorganization process starts. See text for details. The corresponding space–time diagram can be found in figure 5.

simulations of PCF by Lundbladh & Johansson (1991) and by Duguet & Schlatter (2013) in larger domains, from the model flows studied by Schumacher & Eckhardt (2001) and Lagha & Manneville (2007), from the experiments in plane Poiseuille flow by Lemoult, Aider & Wesfreid (2013) and from our own experimental study (Couliou & Monchaux 2015), it appears that large-scale flows are always present around the growing spot. Their origin can be explained by the laminar–turbulent coexistence and

https://doi.org/10.1017/jfm.2017.140 Published online by Cambridge University Press

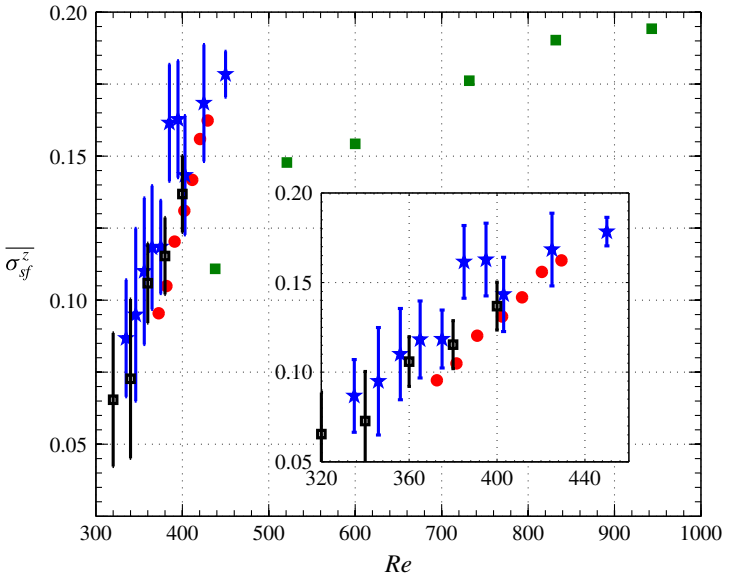


FIGURE 2. (Colour online) Spot spanwise spreading rate $\overline{\sigma_{sf}^z}$ as a function of Re from Tillmark (1995) (green filled squares), Dauchot & Daviaud (1995) (red filled circles), our experiment (black open squares with error bars) and our numerical simulation (blue filled stars with error bars). Note that $\overline{\sigma_{sf}^z}$ is defined in the present article as the temporal average of half the total spot spanwise growth rate, or equivalently as the average of both spanwise front velocities. Other authors' data have been obtained graphically from their publications and scaled to comply with the present definition of $\overline{\sigma_{sf}^z}$.

more particularly by the streamwise flow-rate mismatch occurring in the overhang region where the laminar flow on one wall faces turbulent flow on the other wall (Coles 1965; Lundbladh & Johansson 1991). The actual shape of large-scale flows depends on the wall-normal plane of observation, but they are globally oriented in the spanwise direction, and are outward at the spot spanwise tips and in the streamwise direction and inward at the spot streamwise tips. Experimental works already cited also report the existence of waves at the spot spanwise tips. These waves may correspond to the advection of streamwise vortices that are actually visible on the snapshots presented in figure 1 and that have been observed from visualizations in spanwise–wall-normal planes by Hegseth (1996). Both these features are thought to be relevant in understanding the spot spanwise growth dynamics. Following the work of Gad-El-Hak, Blackwelderf & Riley (1981) on the boundary layer, the spot spanwise growth is usually attributed to local instabilities of the modified laminar profile at the spanwise laminar–turbulent interface (Dauchot & Daviaud 1995; Hegseth 1996). Schumacher & Eckhardt (2001) emphasize the fact that suppressing the large-scale recirculation in the parallel flow of interest in their work inhibits the spot growth. The same conclusion may also hold for plane Couette flow. Trying to select the most meaningful features, Duguet, Le Maître & Schlatter (2011) have studied the growth of turbulent spots in narrow domains for which the periodicity in the streamwise direction is achieved at a wavelength shorter than the typical spot streamwise extent. By doing so, the large-scale recirculation is suppressed and the authors found a stochastic growth resulting from the competition between streak retreat and generation events. The corresponding growth rates are found to be one order of magnitude lower

https://doi.org/10.1017/jfm.2017.140 Published online by Cambridge University Press

than those usually measured in domains extended in both directions. It is nevertheless difficult to know if this stochastic growth is actually active in such large domains since the stochastic growth rate could be smaller than the measurement uncertainties on the total growth rate. The role of large-scale flows can primarily be seen as a disturbance to the stable laminar profile around the turbulent spot. The temporal evolution of the large-scale flows is quite slow as compared to the rapid turbulent fluctuations and happens on the same order of time scales as those associated with the spot growth, as shown for example in our experimental study Couliou & Monchaux (2015) or a recent model by Manneville (2015). As a result, the large-scale flows may induce modifications to the laminar flow around the turbulent spot that are strong enough to turn this profile unstable and steady enough to allow the instability to develop. The local corresponding mechanism is the growth by destabilization we alluded to above. A quantitative study of this mechanism has been undertaken in plane Poiseuille flow by Henningson, Johansson & Alfredsson (1994), but the growth rate was found to be too small to fully explain the experimentally observed rapid expansion of turbulent spots. If relevant, the two mechanisms we have just described are not sufficient and should be only part of the growth process. In a recent article (Couliou & Monchaux 2016), we have shown the existence of two localizations for the generations of new streaks occurring during the spot growth. We have attributed these two localizations to two different mechanisms. The first one is local, happens at the spanwise tips of the growing spot and results in the nucleation of new streaks at the laminar–turbulent interface, outside of the turbulent region. It could result from instabilities of the modified laminar flow as explained above or from the stochastic process revealed by Duguet *et al.* (2011). The second mechanism was actually shown by our study. It occurs globally and is induced by an advection due to the large-scale flows present around the spot that tend to spread it in the spanwise direction. A first consequence of this spreading is a temporary widening of the streaks constituting the turbulent spot before a new streak is nucleated by some wavelength instability inside the turbulent phase to restore the favoured state consisting of more or less equally spaced streaks.

The spot growth process results from the interplay between several mechanisms and involves large-scale flows. Isolating each mechanism and quantifying its contribution to the total growth rate now seems possible. In the present article, the temporal aspects of spot spreading are investigated in order to quantify the extent to which the two identified growth mechanisms are present and interact to achieve the time-averaged results which we have presented in our earlier work (Couliou & Monchaux 2016). To do so, we analyse experimental and numerical data, the acquisition and post-processing of which will be described in § 2. The main results consist of growth rates, front velocities and large-scale flow measurements that are gathered in § 3. Discussion of these results is given in § 4 before we summarize our findings and identify perspectives of this work in § 5.

2. Methods

In this section, we present our experimental set-up, the numerical code used to perform the direct numerical simulations (DNS), the protocols used to trigger the turbulent spots, the measurement and visualization systems and the various post-processing techniques applied to our data.

2.1. *Experimental set-up*

As sketched in figure 3(*a*), an endless 0.25 mm thick plastic belt is stretched between two cylinders. One of them is connected to a brushless servo-motor which drives

https://doi.org/10.1017/jfm.2017.140 Published online by Cambridge University Press

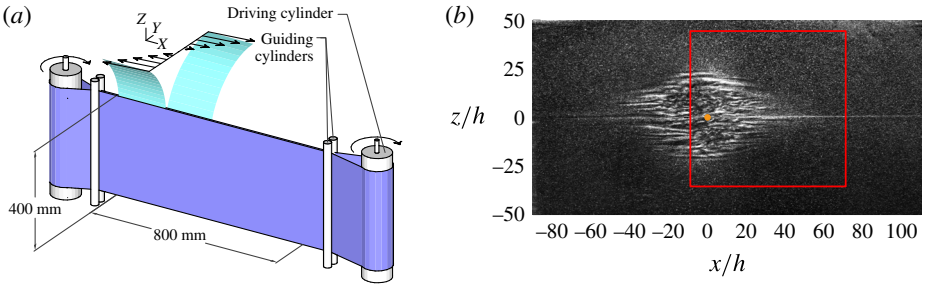


FIGURE 3. (Colour online) (*a*) General sketch of the plane Couette flow set-up. (*b*) Snapshot obtained from our visualization system during the growth of the turbulent spot. The window for particle image velocimetry is highlighted by the red frame. The orange dot corresponds to the position of the bead.

the system through a gear reducer of ratio 9. This motor can achieve a maximal speed of 2500 rpm. Speed and acceleration are controlled to an accuracy of 2/1000. Four smaller cylinders guide the belt and enable one to adjust the gap between the two walls moving in opposite directions at an accuracy of 0.05 mm. All the results presented here correspond to a gap of $2h = 7.5$ mm. This set-up is immersed in a tank filled with water. The water temperature is monitored by a thermocouple with a 0.5 °C accuracy. The Reynolds number is defined as $Re = Uh/\nu$, where ν is the kinematic viscosity of the fluid, U the belt velocity and h the half-gap between the two faces of the belt. The uncertainties on the belt velocity, the gap width and the temperature lead to an Re uncertainty of 5. The x, y and z directions are respectively the streamwise, wall-normal and spanwise directions, and U_x, U_y and U_z are the associated velocities. Owing to the experimental geometry, the plane Couette profile is achieved within an area of size $L_x \times L_z = 800$ mm $\times$ 400 mm, which is our visualization field of view. The corresponding aspect ratios are $\Gamma_x = L_x/h = 107$ and $\Gamma_z = L_z/h = 53$. The plane $y = 0$ is midway between the two plates. The tank is closed at the top by a transparent Plexiglas lid wherever the plane Couette profile is achieved in order to enable top and bottom symmetrical boundary conditions. From previous experiments not detailed here, the critical Reynolds numbers have been obtained as $R_g \simeq 305$ and $R_t \simeq 390$, which are consistent with previous experiments and well-resolved DNS.

2.2. *Experimental protocol*

The flow is permanently perturbed by a bead positioned close to the $y = 0.5h$ plane at $(x, z) = (0, 0)$ corresponding to the centre of the experiment. The bead is maintained by means of a thin wire stretched between two stalks placed between and aligned with the guiding and main cylinders as illustrated in figure 4. This type of permanent perturbation was used by Bottin, Dauchot & Daviaud (1997). The wire diameter is $\phi_{wire}/h = 0.1$ and the bead diameter is $\phi_{bead}/h = 0.8$. As explained in Bottin *et al.* (1998), a thin wire parallel to the streamwise direction does not influence the flow since it does not induce any wake formation. The bead diameter does not strongly affect the qualitative results and, provided that $Re > Re_g$, no intermittency is observed and the bead is rather only triggering turbulent spots. We studied the influence of the stalks and wire on the transition to turbulence in our system when the bead is not present: their influence is hardly noticeable when considering critical Reynolds numbers and transition time to turbulence. When turbulence develops in a formerly

https://doi.org/10.1017/jfm.2017.140 Published online by Cambridge University Press

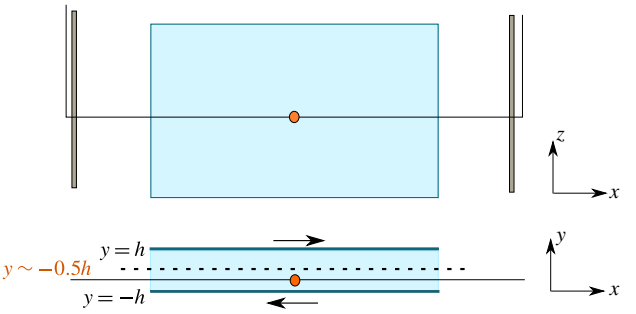


FIGURE 4. (Colour online) Side and top sketches of the perturbation set-up.

laminar domain, it always occurs first around the bead. A typical experiment is a step consisting of a sudden increase of Re from 0 to a final Reynolds number Re_f. The acceleration used is such that the belt reaches its final velocity in less than 0.3 s, i.e. less than $10h/U$, which is always very short as compared to the spot development time scales. For each kind of experiment (final Re value Re_f, presence of the bead or not, ...), we have performed from five to 10 independent realizations. Unless otherwise specified, the results presented here are ensemble-averaged over these different realizations.

2.3. *Particle image velocimetry measurements and visualizations*

Velocity measurements have been achieved by particle image velocimetry (PIV). The Dantec system consists of a dual-pulse Nd:YAG laser (2×135 mJ, 4 ns, 532 nm) and a charge-coupled device (CCD) camera (FlowSenseEO, 4 Mpx). Image pairs are acquired at a rate of 5 Hz. The PIV laser is mounted above the test section on a linear traverse such that velocities over different y planes can be measured with a spatial resolution of approximately 1.3 mm along y. The laser sheet produced from a cylindrical lens gives two-dimensional velocity fields (U_x, U_z) in the streamwise–spanwise planes. The flow is seeded with Rhodamine-coated particles that diffuse light at a shifted wavelength. Their diameter d_p is in the range 1–20 mm. A filter mounted on the camera lens is used to keep only wavelengths around this shifted wavelength, getting rid of unwanted light reflections on the vessel and plastic belt. The 1948 pixel $\times$ 2048 pixel observation window corresponds to physical sizes of 305 mm $\times$ 310 mm. An adaptive cross-correlation processing is applied to an initial interrogation area of 64 pixel $\times$ 64 pixel followed by a final interrogation area of 32 pixel $\times$ 32 pixel with 50 % overlap. The corresponding spatial resolution is 2.45 mm, i.e. $0.6h$. Each instantaneous velocity field is further filtered by removing values exceeding $1.2U$. Resulting outliers are replaced using local median filters.

Alternatively, visualizations are performed over the entire area where a plane Couette flow is achieved. To that purpose, the flow is seeded with Iriodin particles and illuminated with a laser diode combined with a polygonal mirror rotating at high frequency to produce a laser sheet which illuminates the flow along a plane at a given y. Iriodin particles are micrometre-sized platelets which tend to align with the flow stream. These platelets respond to local flow changes and reveal laminar and turbulent regions: the turbulent state is indicated by quick fluctuations in the reflected light intensity, while the laminar state corresponds to more uniform light reflections. Images at a resolution of approximately 2200 pixel $\times$ 1100 pixel, corresponding to an

https://doi.org/10.1017/jfm.2017.140 Published online by Cambridge University Press

observation window of 800 mm × 400 mm (exactly fitting the area where the laminar Couette profile is achieved), are captured by a PCO sCMOS camera provided by PhotonLine. Figure 3(*b*) illustrates typical full-size visualizations with both laminar and turbulent phases coexisting.

The growth of turbulent spots in the whole flow is obtained from visualizations and will be presented in § 3.2. PIV measurements are used to study large-scale flows; associated results will be presented in § 3.4. For practical reasons, it is not possible to perform PIV measurements and visualizations at the same time. As a consequence, from the experimental data, it will not be possible to match the time evolution of large-scale flows and of spot growth. We will thus mostly rely on the numerical data for such comparisons.

2.4. *Direct numerical simulations*

DNS of a plane Couette flow are computed using the Channelflow software written by J. F. Gibson (Gibson, Halcrow & Cvitanović 2008; Gibson 2014). The software solves Navier–Stokes equations numerically by using pseudo-spectral methods for the spatial discretization with a Fourier decomposition in the (x, z) directions and Chebyshev polynomials in the y direction. The boundary conditions are periodic in the (x, z) directions and no-slip conditions are imposed at the walls, i.e. at $y = \pm 1$. Numerical simulations are performed in a domain of size $(L_x, L_y, L_z) = (180, 2, 80)h$. In order to resolve all the relevant modes of turbulent flow in the Re range studied, the numerical resolution is (768, 33, 384) dealiased modes in the (x, y, z) directions. According to Philip & Manneville (2011) this is sufficient to observe pattern formation. A time step of 0.01 was used, resulting in a Courant–Friedrichs–Lewy (CFL) number less than 0.6. A perturbation consisting of four pairs of counter-rotating vortices like that used by Lundbladh & Johansson (1991) is introduced as an initial disturbance to trigger turbulent spots. As for the experiment, five realizations of the DNS have been performed for each Re value and ensemble-averaged results are presented. Note that, for the DNS, a slight change in the perturbation amplitude (typically 0.1 %) is introduced to achieve some variability between realizations.

2.5. *Space–time diagrams and front detection*

A large part of the results presented in the next section are obtained from space–time diagrams drawn from both numerical and experimental data. They are obtained from the dimensionless streamwise velocity component U_x/U extracted on the line $(x, y) = (0, 0)$ in the numerical case and from the $x = 0$ line-of-light intensity acquired by our visualization system in the experimental case. To strengthen the detected structures and in order to improve the signal-to-noise ratio, sliding averages are applied along the x coordinates over three samples and along the time coordinate over five samples. Typical examples of numerical and experimental space–time diagrams are provided in figure 5.

Laminar–turbulent fronts are manually tracked in the experiment and automatically detected from the numerical data by defining two possible states: the laminar one, which corresponds to the area where $U_x = 0$; and the turbulent state, which corresponds to the remaining area. We focus on the spanwise expansion on line $x = 0$, and one can note that at this location the large-scale flow is mainly oriented towards z and is consequently not that visible from U_x.

2.6. *Large-scale flows*

As reported by many authors (see § 1), large-scale flows develop around growing turbulent spots in shear flows. They are easily identified by studying the two-

https://doi.org/10.1017/jfm.2017.140 Published online by Cambridge University Press

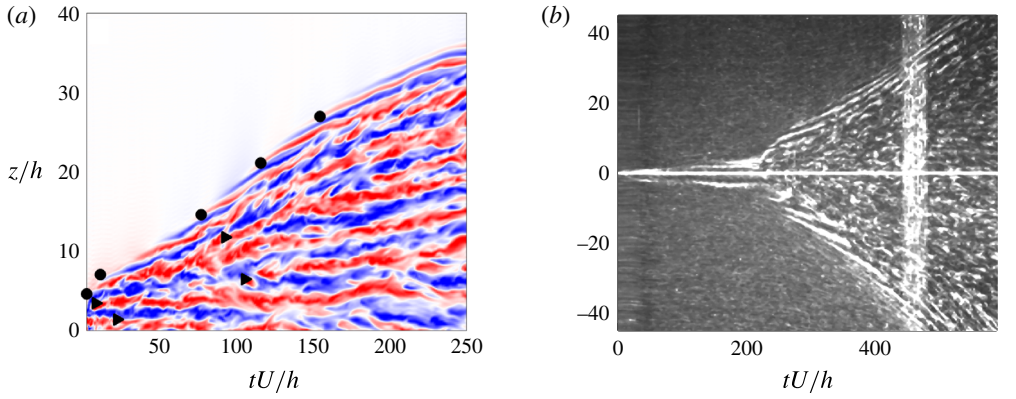


FIGURE 5. (Colour online) (*a*) The U_x/U space–time diagram for a DNS at $Re = 380$. Nucleations of streaks inside (triangles) and outside (circles) of the spot are marked. Only half the spot is presented in the spanwise direction. Blue, negative velocities; red, positive velocities; and white, zero velocity. (*b*) Space–time diagram from the experimental visualization corresponding to the growing spot presented in figure 1. The final $Re = 403$ is reached after $10h/U$ and, according to Tillmark & Alfredsson (1992), the linear Couette profile is established after approximately $0.25Re\,h/U$ corresponding to $100h/U$ in this case. The white vertical band from $450h/U$ to $480h/U$ corresponds to the tape which closes the plastic belt.

dimensional spatial power spectrum of either velocity component in the (x, z) plane. These power spectra show an obvious scale separation between two peaks; one occurs around the wavelength $\lambda \simeq (4\text{–}5)h$ corresponding to turbulent streaks, and another one, associated with large-scale flows, is situated around $\lambda = 40h$ (Tuckerman, Barkley & Dauchot 2008; Duguet & Schlatter 2013; Couliou & Monchaux 2015). In this work, we will use two quantities associated with large-scale flows: $A_z^{LSF} = kE_z(\lambda = 40h)/U^2$, which represents the U_z premultiplied power spectra amplitude at $\lambda = 40h$; and $M_z^{LSF} = \max(\widehat{U}_z(x = 0,\ y = 0,\ z),\ z)$, the maximal amplitude of $\widehat{U}_z$, which is the spanwise velocity component filtered above the cutoff wavelength $\lambda_{cut} = 24h$ on the line $x = 0$, $y = 0$. More details can be found in the work by Couliou & Monchaux (2015).

3. Results

3.1. *General features*

3.1.1. *Growth time scales and region definition*

Owing to our numerical and experimental protocols, the growth of the triggered spot differs slightly in the two cases presented in figure 5. In the numerics, a turbulent zone is established very quickly (few h/U) from the initial perturbation that is already large, of the order of $5h$. The spot growth in our experiment takes place in two phases, as can be seen in the space–time diagram of figure 5(*b*). During a first phase lasting $t_p h/U$ (t_p being approximately 210 in the displayed example), structures develop around the bead. Then an actual spot, with an interior made of turbulent fluctuations like the ones displayed in any numerical or experimental study of such spots, grows until the end of the acquisition. In the experimental case, as our step protocol starts at $Re = 0$, a time t_c is required for the laminar profile to establish itself. An important point is to know how the time t_c compares to t_p associated with the development of the perturbation before turbulence is triggered. According to

https://doi.org/10.1017/jfm.2017.140 Published online by Cambridge University Press

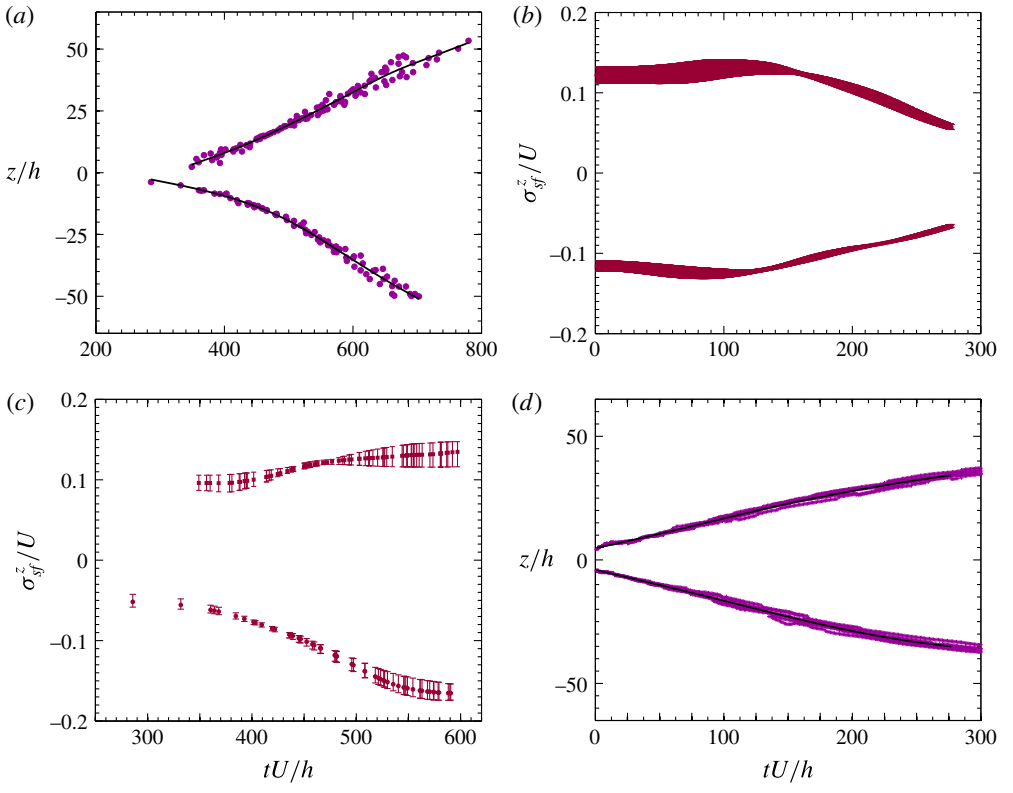


FIGURE 6. (Colour online) Methodology. (*a*) Front position (dots) and corresponding smoothing spline (black lines) from an experiment at $Re = 365$. (*d*) Same as (*a*) in a numerical simulation at $Re = 380$. (*c*) Front velocities obtained by differentiating the cubic spline of (*a*). (*b*) Front velocities obtained by differentiating the cubic spline of (*d*).

measurements performed by Tillmark and reported in Tillmark & Alfredsson (1992), the linear Couette velocity profile is established in a time $t_c \simeq 0.25\,Re\,h/U$. In our experiment, this corresponds to a time of the order of $100h/U$, which is short enough as compared to $210h/U$ when the spot is triggered.

The experimental space–time diagram presented in figure 5(*b*) allows us to define three distinct zones during the growth of a turbulent spot. The region connected to the bead is turbulent and displays fluctuating disorganized structures. Far away from the bead, the flow is laminar, which results in roughly homogeneous dark areas. Between these two regions, long coherent inclined structures are visible. They correspond to the waves evoked by many authors, as explained in § 1, and it has been argued that these waves correspond to the advection of streamwise vortices by the large-scale flows present at the spot spanwise tips (Couliou & Monchaux 2016). A similar distinction is actually also observed on the numerical space–time diagram.

3.1.2. *From fronts to spreading rate*

The spanwise fronts of the turbulent spot are tracked to measure the spot front velocity. From the individual fronts detected manually from the experiment and automatically from the DNS as explained in § 2.5, we obtain scatter plots such as those presented in figure 6(*a*,*d*) that provide the front position as a function of time

https://doi.org/10.1017/jfm.2017.140 Published online by Cambridge University Press

for each experiment or simulation. In the experimental case, the time at which the spot starts growing may vary from one realization to another. To obtain the scatter plot presented in figure 6(*a*), we have translated each front so that the fronts coincide when they have reached $z = \pm 16h$. Note that, when $Re < 320$, it may happen that no spot grows in some cases. The results presented in the following are obtained by gathering fronts associated with spots that eventually grow. In both numerical and experimental scatter plots, gathering from five to 10 independent realizations, the dispersion between different spot fronts is small enough such that an average front can be obviously distinguished. The position of this average front is obtained from cubic spline interpolation with a smoothing parameter μ. This cubic spline is further differentiated to obtain the average front velocity, i.e. half the average spot spreading rate, as a function of time at a given Re. In practice, we perform this velocity calculation by regularly varying the smoothing parameter μ from 0.5 to 0.9. We thus obtain several time velocity signals that differ slightly from one another. The ensemble average of these velocity signals is used as the spot front velocity and their ensemble standard deviation as the corresponding error bar. Figure 6(*c*) presents such a velocity signal and its error bar for $Re = 365$. We can also appreciate in figure 6(*c*) the relative symmetry of both fronts (top and bottom of the experiment) that is representative of the symmetry obtained at any Re. Note that the numerical front velocity signals are not found to be more symmetric than the experimental ones, even though the numerical boundary conditions are perfectly symmetric. The consequences are twofold: the top–bottom symmetry is fairly preserved in our experimental set-up; and the remaining asymmetry in the growth dynamics has to be attributed to the dynamics itself and not to the boundary conditions.

3.1.3. *Velocities of edge vortices*

From experimental space–time diagrams such as the one presented in figure 5(*b*), the edge vortices are manually detected as straight lines. Their individual velocity is then estimated as the corresponding slope. For a given Re, all detected velocities of the vortices are gathered in a scatter plot as done in figure 6 for spot fronts. It appears that, as time passes, the velocity increases linearly and a linear fit of the scatter plot is thus performed.

3.1.4. *Quantities of interest and relation to growth mechanisms*

To study the spreading dynamics, we consider four quantities: σ^z_{sf}, the velocity of the spot front; σ^z_{adv}, the velocity of the vortices; σ^z_{loc}, defined as $\sigma^z_{sf} - \sigma^z_{adv}$; and the ratio $\sigma^z_{loc}/\sigma^z_{sf}$. All these quantities depend on time and Re. Their time averages have been studied by Couliou & Monchaux (2015) to reveal the two growth mechanisms described in the introduction: σ^z_{sf} corresponds to the spot spreading rate in the spanwise direction; σ^z_{adv} is associated with the global growth induced by large-scale flows and corresponds to the rate of streak nucleations inside the turbulent spot. From its definition, if only these two mechanisms are at work, σ^z_{loc} measures the importance of the local mechanism and corresponds to the rate of streak nucleations outside the turbulent region. The ratio $\sigma^z_{loc}/\sigma^z_{sf}$ simply quantifies the relative importance of both mechanisms and can be compared to the fraction of nucleations occurring outside or inside the turbulent spot, which can be obtained from the numerical data. Next we present the time dependence of these four quantities in our experiments and in our simulations. In the sequel, $\overline{X}$ will denote the time average of the quantity X. The different quantities defined above are collected in table 1.

https://doi.org/10.1017/jfm.2017.140 Published online by Cambridge University Press

Quantity	Definition	Measurement
σ_{sf}	Total growth rate of the spot	From laminar–turbulent front velocity
σ_{adv}	Growth rate fraction due to advection	From the velocity of edge vortices
σ_{loc}	Remaining growth rate fraction	As difference $\sigma_{sf} - \sigma_{adv}$

TABLE 1. The different growth rates used in the text, their definitions and the ways they are measured.

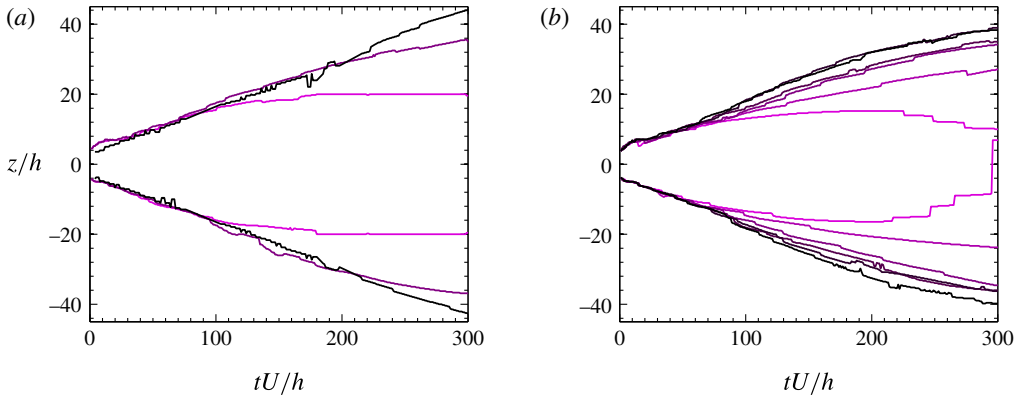


FIGURE 7. (Colour online) Methodology. (*a*) Front position for three numerical simulations performed at $Re = 380$ for three different domain sizes ($L_x \times L_z = 360h \times 160h$, $L_x \times L_z = 180h \times 80h$ and $L_x \times L_z = 90h \times 40h$). Lightest lines correspond to smaller boxes. (*b*) Superposition of all fronts obtained at various Re by numerical simulations for a domain size of $L_x \times L_z = 180h \times 80h$. From brightest to darkest, Re increases from 320 to 420 in steps of 20.

3.1.5. *Influence of box size and reproducibility*

Figure 7(*a*) illustrates the spot fronts for three numerical simulations performed at the same Reynolds number $Re = 380$ but with increasing box sizes at constant aspect ratio. The darkest line corresponds to the spot fronts for a larger box, and the brightest line corresponds to a smaller box than that used here. It appears that the influence of the box size is negligible at the beginning of the growth, but becomes significant at later times when the effect of the periodic boundary conditions on the spot front is no longer negligible. In order to avoid any bias from this size effect, we have decided to study the spot growth dynamics before the box size influences the spot development. More specifically, the recording of the front position should be stopped when it reaches $\pm 36h$ with our box size. The same restriction has been applied to our experimental data.

Figure 7(*b*) illustrates the average spot fronts for the six Reynolds numbers studied numerically. It appears that one quarter of the dynamics are identical, regardless of the Reynolds number and even when the spot eventually vanishes (see the brightest lines corresponding to $Re = 320$). During this first phase, the spot growth rate is roughly independent of Re and so are the mechanisms responsible for the spot spreading that can possibly involve non-normal growth.

https://doi.org/10.1017/jfm.2017.140 Published online by Cambridge University Press

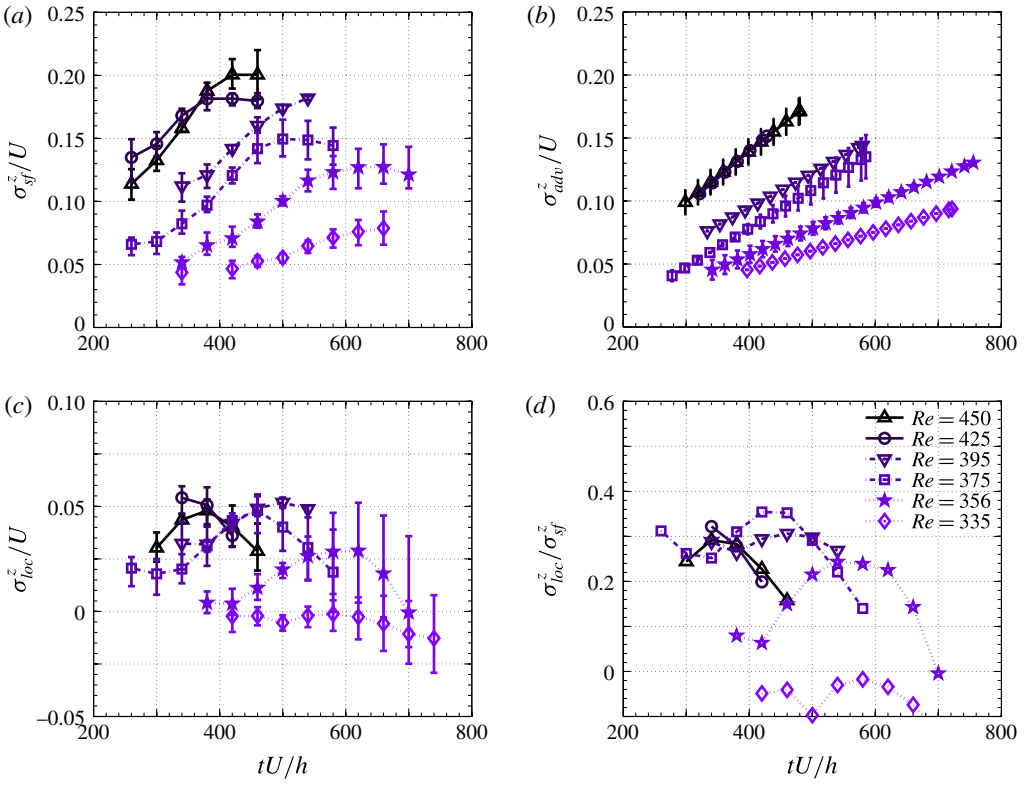


FIGURE 8. (Colour online) Total spot growth rate σ^z_{sf} (*a*), edge vortices advection velocity/advective growth rate σ^z_{adv} (*b*), local growth rate σ^z_{loc} (*c*) and ratio $\sigma^z_{loc}/\sigma^z_{sf}$ (*d*) as functions of time for various *Re*. Experimental data.

3.2. *Spreading in experiments*

Figure 8 illustrates the time evolution of the four quantities defined in table 1 for six values of the Reynolds number spanning the range of *Re* studied here. We do not present the 11 available *Re* values for the sake of clarity but the limiting cases detailed below take them into account.

In figure 8(*a*), σ^z_{sf} is seen to increase monotonically with time, while saturating at the end of the growth, resulting in S-shaped curves whose typical amplitude is $0.13U$. When varying the Reynolds number, the overall shape of these curves does not change, but their starting point is higher and occurs at earlier time for larger *Re* so that they can be deduced from one another by simple translations. The spot growth is faster at larger *Re* and, with the type of perturbation used here, it also starts earlier, even in dimensionless units. This is probably due to faster development of the perturbation around the bead in the first stages of the experiment (see § 2.2).

In figure 8(*b*), σ^z_{adv}, the velocity of the vortices, is seen to increase linearly with time. The rate of this increase grows with the Reynolds number, so that, at the end of the growth process, vortices travel much faster at larger *Re*, while in the first steps of the growth dynamics, all vortices go roughly at the same speed ($0.05U$ within our measurement accuracy), except at very large *Re* values. Note that the time span on which the velocity of the vortices is displayed is different from the displayed time span for the spot front position. This is because vortices are not always found in the

https://doi.org/10.1017/jfm.2017.140 Published online by Cambridge University Press

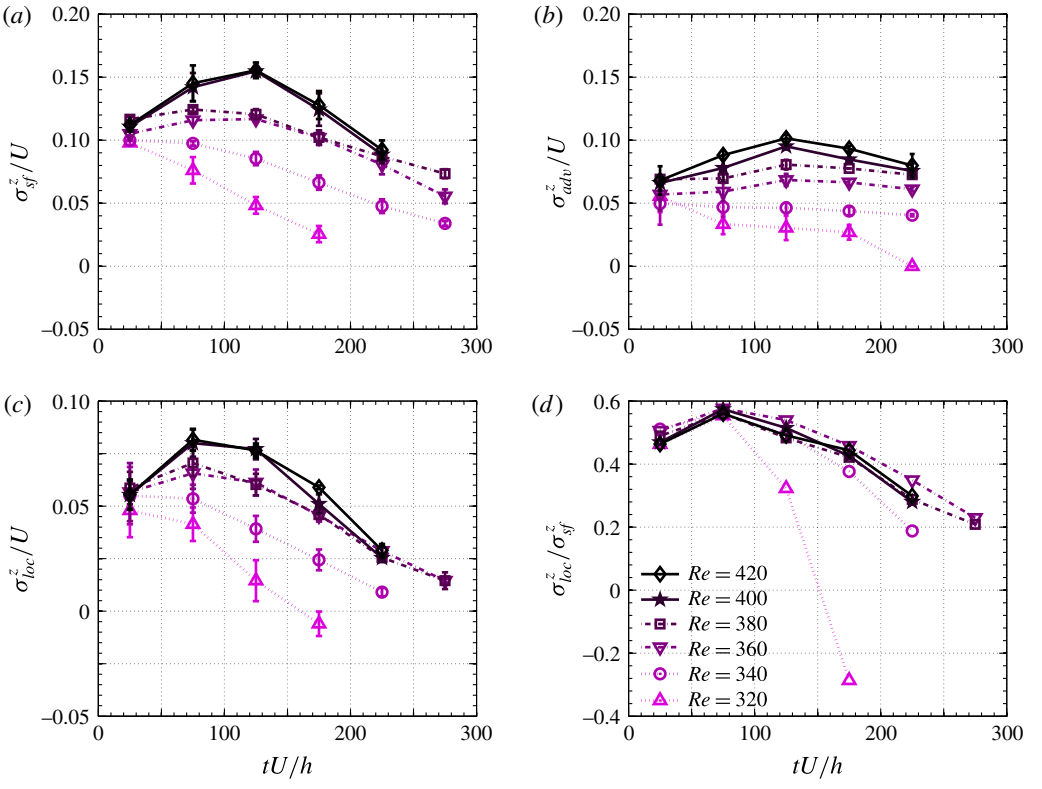


FIGURE 9. (Colour online) Total spot growth rate σ^z_{sf} (a), edge vortices advection velocity/advective growth rate σ^z_{adv} (b), local growth rate σ^z_{loc} (c) and ratio $\sigma^z_{loc}/\sigma^z_{sf}$ (d) as functions of time for various Re. Numerical data.

space–time diagram at all times, either because they are not present, or because the visualization quality does not allow us to accurately track them. As σ^z_{loc} and $\sigma^z_{loc}/\sigma^z_{sf}$ are derived from σ^z_{adv}, the same remark obviously applies for them too.

Owing to the different dependences for σ^z_{sf} and σ^z_{adv} on Re, their difference σ^z_{loc} has more complicated dynamics that strongly depends on Re. The local contribution to the total growth is most of the time between 10 % and 30 % at any Re. This shows that most of the spot growth has to be attributed to the global mechanism, as already proven from the time-average study by Couliou & Monchaux (2015).

3.3. *Spreading in numerics*

Figure 9 gathers the time evolution of the three growth rates defined above and of their ratio for different Reynolds numbers in the numerical simulations. As a preliminary remark, we can note that all these figures differ from the experimental ones. Precise differences will be explained in this section. Note that for $Re = 320$, spots grow during a first phase but eventually vanish. For $Re = 340$, spots arise in most cases but their sizes stay moderate and fluctuate.

Contrary to what was observed in the experiment, the behaviour of σ^z_{sf} strongly depends on Re. For $Re > 360$, its maximum is reached at approximately $125h/U$. Below this value, σ^z_{sf} decreases monotonically with time and the decreasing rate is

https://doi.org/10.1017/jfm.2017.140 Published online by Cambridge University Press

stronger with lower Reynolds number. Note that, for $Re = 320$, the spreading rate ends up negative since the considered spot actually vanishes (not presented). Regardless of the Reynolds number, the total growth rate σ^z_{sf} is of the order of $0.12U$ at short times and takes values between $0.05U$ and $0.15U$. This order of magnitude is similar to the experimental one.

The quantity σ^z_{adv} also displays a dynamics that is more complicated than in the experimental case and that is *Re*-dependent. It is roughly constant at low *Re*, slowly increasing at intermediate *Re* values but presents a maximum for larger *Re*. This maximum is once again reached around $125h/U$. Regarding the orders of magnitude, they increase with *Re* from $0.05U$ to $0.1U$. Once again, this order of magnitude is similar to the experimental one, although slightly smaller for larger *Re*.

The quantity σ^z_{loc} has time and *Re* dependences very similar to that of σ^z_{sf}, except that the maxima are reached at earlier times. As in the experimental case, its order of magnitude is around $0.05U$.

The trends of $\sigma^z_{loc}/\sigma^z_{sf}$ are almost identical regardless of the Reynolds number. They increase with time from values around 50 %–60 % in the early stage of the growth before decreasing down to values around 20 %. The order of magnitude is clearly smaller than in the experimental case.

Coming back to the underlying mechanisms, these numerical results show that the global growth induced by large-scale flows dominates the growth rate at long times while local growth is much more active at the beginning of the growth process, leading to a balance between the two mechanisms. It is interesting to note that, when comparing the orders of magnitude seen in the experiment and in the simulation, they are very similar for the local growth (σ^z_{loc}) but clearly larger in the experiment for the global growth (σ^z_{adv}). This will be further discussed in § 4.

3.4. *Large-scale flows*

As explained in § 2, large-scale flows and spot growth are not measured experimentally during the same experiment. Thus a straightforward temporal comparison of the associated dynamics is not possible. We have chosen to time-shift the large-scale flow quantities so that time $t = 0$ corresponds to early stage of the growth presented above, at around one quarter of the overall process.

In § 2.6, we have introduced two quantities associated with large-scale flows: A^{LSF}_z and M^{LSF}_z. The quantity A^{LSF}_z gives a global measure of the large-scale flow amplitude while the quantity M^{LSF}_z is a local direct estimation of the order of magnitude of the advection of edge vortices by large-scale flows (see § 1). Figure 10(*a*,*c*) illustrates the evolution of these global and local measurements in our experiment on time scales relevant to the growth process as explained above. Both have relatively similar time dependences. At low *Re*, they are fluctuating around a low constant value during the whole growth process. When $Re > 330$, they increase from the beginning of the growth process and then saturate or slowly decay (actually, at later non-represented times, they all decay). For higher values of *Re*, the increase is faster and the decay starts sooner. Similar observations can be made for the numerical data presented in figure 10(*b*,*d*). The maximum of $\max(U^{LSF}_z)$ is reached at approximately $t \simeq (120\text{–}150)h/U$ when the spot front velocity was found to be maximal too.

4. Discussion

4.1. *Comparison to former work*

The spot front velocity as a function of time for different *Re* is represented in figure 8. Contrary to some of the previous works that found the spot front velocity

https://doi.org/10.1017/jfm.2017.140 Published online by Cambridge University Press

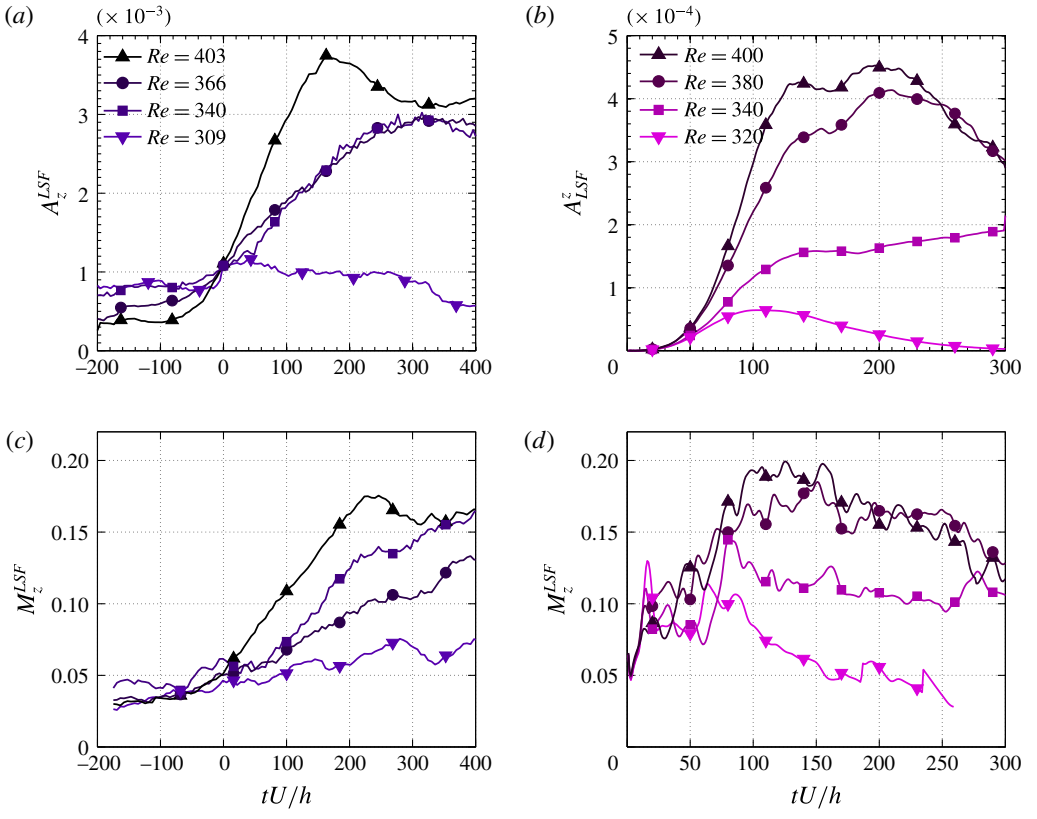


FIGURE 10. (Colour online) Plots of A_z^{LSF} (*a*,*b*) and M_z^{LSF} (*c*,*d*) as a function of time for different *Re* in the experiment (*a*,*c*) and in the DNS (*b*,*d*). See text for precise definitions.

to be independent of time, particularly those by Dauchot & Daviaud (1995) and by Tillmark (1995), these plots show a time-dependent spot front velocity, even if our experimental set-up is very similar to the ones cited. In fact, these researchers have followed spot growth over shorter times and have performed linear fits of the measured spot fronts equivalent to that presented here in figure 6(*a*). Restricting the spot growth presented here to their first part, performing the same linear fitting seems reasonable since the nonlinear evolution clearly appears only when considering the full temporal signal.

On average, the spot front velocity $\overline{\sigma_{sf}^z}$ is found both in our experiment and in our simulations to be of the same order of magnitude as the one presented in Dauchot & Daviaud (1995) even though slightly larger, particularly in the experimental case. The dependence of $\overline{\sigma_{sf}^z}$ on *Re* is nevertheless similar in all cases, as illustrated with the three parallel curves presented in figure 2.

The velocities of edge vortices measured here as a function of both time and *Re* have an order of magnitude similar to those found by Dauchot & Daviaud (1995) and by Tillmark (1995). Unfortunately, the dependences of these velocities with time or Reynolds numbers were not provided, so that the comparisons cannot be pushed further. As we are, to our knowledge, the first to investigate the time evolution of the spot development in plane Couette flow and the link to large-scale flow development, we cannot compare this part of our study to former contributions. The next subsection is dedicated to a discussion of these aspects.

https://doi.org/10.1017/jfm.2017.140 Published online by Cambridge University Press

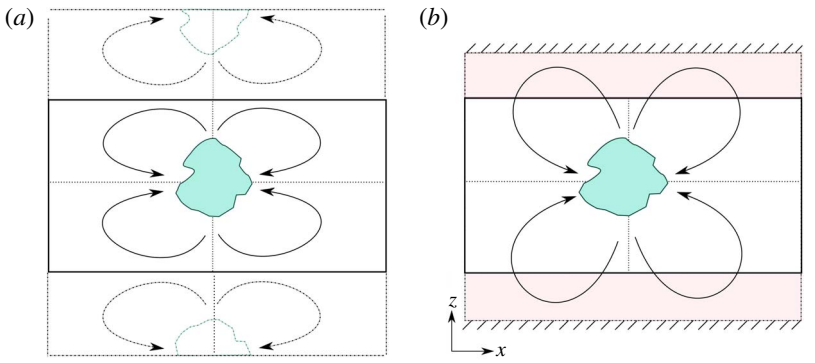


FIGURE 11. (Colour online) Schematic representation of the periodic boundary conditions in numerical simulation (*a*) and of water at rest and wall boundary conditions in the experiment (*b*).

4.2. *Experiments versus numerics*

As already mentioned in the last section, there are differences between the numerical and experimental velocity evolutions presented here. When the numerical domain size is modified, we have seen in § 2 that the growth of turbulent spots is affected. When the spot fronts reach $0.87L_z$, which corresponds to a distance to the domain boundary of $0.13L_z$, the fronts slow down. We have thus restricted our analysis to regions far enough from the domain boundaries in order to limit the influence of this finite-size effect. We have done so for both numerical and experimental data as already explained. Nevertheless, the boundary conditions are very different in both cases, as sketched in figure 11. In simulations they are periodic, while in the experiment they consist of walls where the spanwise velocity vanishes. The distance between these walls and the belt edges is approximately $L_z/7$. A buffer area thus exists between the shear zone and these walls. As a consequence, numerical and experimental fronts are analysed in physical zones of similar sizes but enclosed within very different boundary conditions. The main consequence of these differences is that large-scale flows associated with a numerical spot are tempered by their periodic images at times when, in the experiment, the buffer zone still allows these structures to develop. We indeed observe experimentally that the large-scale recirculation is actually present in the buffer zone as sketched in figure 11. Large-scale flows and thus the spot fronts are slowed down earlier in the numerical simulations than in the experiment. In the experiment, this slowing down should also be observed, but at later times. Since our analysis is restricted to the same physical space in both cases, and since the growth velocities have similar magnitudes, the numerical analysis spans a larger part of the whole dynamics than the experimental one. Indeed, we observe in figure 9(*a*,*b*) that σ^z_{sf} and σ^z_{adv} decrease in the numerical case when they are still increasing in the experimental plots of figure 8(*a*,*b*). Suppressing the buffer area in the experiment should lead to a more similar behaviour.

4.3. *Temporal dynamics*

Considering numerical or experimental data, it is clear that, at any time, both local and global growth mechanisms are at work since σ^z_{adv} and σ^z_{loc} are non-vanishing. Their relative contributions depend mostly on time. The quantities σ^z_{adv} and M^z_{LSF} have

https://doi.org/10.1017/jfm.2017.140 Published online by Cambridge University Press

very similar temporal dynamics: in the experimental case, they are both increasing functions of time and they take values of the same order of magnitude in the range $(0.05–0.17)U$. In the numerical case they exhibit maxima realized at the same time, around $t = 125h/U$. These strong similarities strengthen our conviction that the large-scale flows are responsible for the advection of the edge vortices and of the turbulent spot. From a more quantitative point of view, it is not easy to find a relevant measure of the large-scale flow intensity to be compared to the advection rate σ^z_{adv}. We have used the maximum, which is local and by nature an upper bound. A more refined estimation could be done by an integral measure (over x) at a given distance upstream of the front and over a given streamwise length. This would imply the introduction of two free parameters and could lead to questionable results. Note nevertheless that the large-scale flow maximum is found to strictly remain at a distance $(2–5)h$ upstream of the spot front at any time and for any Re (figure not shown).

4.4. *Growth mechanisms*

Both in our previous work (Couliou & Monchaux 2016) and in the present work we have reported the existence of a global growth mechanism due to advection of the spot by the large-scale flows induced by the laminar–turbulent coexistence. This mechanism is associated with a growth rate σ^z_{adv} that takes non-zero values at any Re and at any time. This implies that large-scale flows are present throughout the growth process, as already shown by direct PIV measurements of these flows by Couliou & Monchaux (2015). As a consequence, the laminar profile outside of the turbulent spot differs from the linear Couette profile at any time and at any Re. A classical hypothesis to explain the growth of turbulent spots is, as detailed in the introduction, a local destabilization of the laminar profile at the spot spanwise tips. With our notation, the corresponding growth rate is σ^z_{loc}. At $Re = 335$, σ^z_{loc} equals zero at any time but large-scale flows are present. The configuration is such that the laminar profile is modified but does not trigger local growth. At $Re = 346$, the local growth is active, as σ^z_{loc} is non-zero. We can thus infer the existence of a critical Re value between 335 and 346 below which the laminar profile modification induced by the large-scale flow is not strong enough to trigger the instability. From the numerical simulations, the modified laminar flow is entirely known and can be extracted to perform linear stability analysis, as was done by Henningson & Alfredsson (1987) for the plane Poiseuille case.

As presented in the introduction, Duguet *et al.* (2011) suggest a local stochastic growth of the turbulent spot. This suggestion comes from observations in narrow domains where associated large-scale flows do not develop. This stochastic growth is associated with a growth rate σ^z_{stoch}, whose order of magnitude is around $0.01U$ in their narrow domains. This is one order of magnitude smaller than the two growth rates introduced in the present work. In fact, Duguet *et al.* (2011) observe numerous streak-retreat events at any Re, while, in our numerical simulations, these events are very rare (five streak retreats over the 35 simulations performed). If this stochastic growth exists in large domains, it cannot explain the measured local growth rate, which, as shown here, contributes to approximately 50 % of the total growth rate.

5. Conclusions and perspectives

Spot growth in the transitional regime of plane Couette flow has previously been studied numerically and experimentally by several researchers, revealing the existence of waves at the spot spanwise tips and pointing out the possible role played by large-scale flows surrounding the developing spot. The actual mechanisms at work to

https://doi.org/10.1017/jfm.2017.140 Published online by Cambridge University Press

achieve the observed growth when *Re* is large enough are still unclear, although most of the former studies suggest a destabilization taking place at the spot spanwise tips. This suggestion is based on results time-averaged over the whole growth process. In our recently published work (Couliou & Monchaux 2016), we have revealed the occurrence of streak nucleation within the turbulent phase pointing to a new global growth mechanism involving large-scale flows. In the present work, we have presented a temporal version of this study showing that the two suggested mechanisms are actually both present throughout the growth dynamics. At all times they contribute significantly to the total growth. Temporal comparison of the global growth rate σ^z_{adv} and of measures of the large-scale flow intensities strengthen our interpretation that the large-scale flows are responsible for the advection of edge vortices and thus for the global spot growth rate. The role of nonlinear advection in the growth of turbulent spots was also noted from a recent model of pipe and channel flows proposed by Barkley *et al.* (2015). From visualizations of both our experiments and simulations, we clearly see that large-scale flows change in shape and intensity during the reorganization occurring when the spot is large enough to form the laminar–turbulent stripe pattern expected at long times. We suggest that they also do play an important role in this reorganization that we have planned to study.

Regarding the spot growth in the streamwise direction, if the same kind of mechanisms act in this direction, due to their geometry, large-scale flows should be acting against the growth in this case. We are currently investigating these aspects from the data presented here. As plane Couette flow shares most of its features with the other extended shear flows, including the existence of large-scale flows around turbulent patches, it is worth performing the same analysis in plane Poiseuille and Taylor–Couette flows to see if the same conclusions can be formulated.

Acknowledgement

This project was supported by ANR Jeunes Chercheurs/Jeunes Chercheuses QANCOUET.

REFERENCES

BARKLEY, D., SONG, B., MUKUND, V., LEMOULT, G., AVILA, M. & HOF, B. 2015 The rise of fully turbulent flow. *Nature* **526**, 550–553.

BARKLEY, D. & TUCKERMAN, L. S. 2005 Computational study of turbulent–laminar patterns in Couette flow. *Phys. Rev. Lett.* **94**, 014502.

BARKLEY, D. & TUCKERMAN, L. S. 2007 Mean flow of turbulent–laminar patterns in plane Couette flow. *J. Fluid Mech.* **576**, 109–137.

BOTTIN, S., DAUCHOT, O. & DAVIAUD, F. 1997 Intermittency in a locally forced plane Couette flow. *Phys. Rev. Lett.* **79**, 4377.

BOTTIN, S., DAUCHOT, O., DAVIAUD, F. & MANNEVILLE, P. 1998 Experimental evidence of streamwise vortices as finite amplitude solutions in transitional plane Couette flow. *Phys. Fluids* **10**, 2597–2607.

CHANTRY, M., TUCKERMAN, L. S. & BARKLEY, D. 2016 Turbulent–laminar patterns in shear flows without walls. *J. Fluid Mech.* **791**, R8.

COLES, D. 1965 Transition in circular Couette flow. *J. Fluid Mech.* **21**, 385–425.

COULIOU, M. & MONCHAUX, R. 2015 Large scale flows in transitional plane Couette flow: a key ingredient of the spot growth mechanism. *Phys. Fluids* **27**, 034101.

COULIOU, M. & MONCHAUX, R. 2016 Spreading of turbulence in plane Couette flow. *Phys. Rev.* E **93**, 013108.

https://doi.org/10.1017/jfm.2017.140 Published online by Cambridge University Press

DAUCHOT, O. & DAVIAUD, F. 1995 Finite amplitude perturbation and spots growth mechanism in plane Couette flow. *Phys. Fluids* **7**, 335–343.

DUGUET, Y., LE MAÎTRE, O. & SCHLATTER, P. 2011 Stochastic and deterministic motion of a laminar–turbulent front in a spanwisely extended Couette flow. *Phys. Rev.* E **84**, 066315.

DUGUET, Y. & SCHLATTER, P. 2013 Oblique laminar–turbulent interfaces in plane shear flows. *Phys. Rev. Lett.* **110**, 034502.

DUGUET, Y., SCHLATTER, P. & HENNINGSON, D. S. 2010 Formation of turbulent patterns near the onset of transition in plane Couette flow. *J. Fluid Mech.* **650**, 119–129.

EMMONS, H. W. 1951 The laminar–turbulent transition in a boundary layer. Part 1. *J. Aerosp. Sci.* **18**, 490–498.

GAD-EL-HAK, M., BLACKWELDERF, R. F. & RILEY, J. 1981 On the growth of turbulent regions in laminar boundary layers. *J. Fluid Mech.* **110**, 73–95.

GIBSON, J. F. 2014 Channelflow: a spectral Navier–Stokes simulator in C^{++}. *Tech. Rep.* University of New Hampshire; Channelflow.org.

GIBSON, J. F., HALCROW, J. & CVITANOVIĆ, P. 2008 Visualizing the geometry of state space in plane Couette flow. *J. Fluid Mech.* **611**, 107–130.

HASHIMOTO, S., HASOBE, A., TSUKAHARA, T., KAWAGUCHI, Y. & KAWAMURA, H. 2009 An experimental study on turbulent-stripe structure in transitional channel flow. In *Proceedings of the Sixth International Symposium on Turbulence, Heat and Mass Transfer* (ed. K. Hanjalić, Y. Nagano & S. Jakirlić), pp. 193–196. Begell House.

HEGSETH, J. J. 1996 Turbulent spots in plane Couette flow. *Phys. Rev.* E **54**, 4915–4923.

HENNINGSON, D. S. & ALFREDSSON, P. H. 1987 The wave structure of turbulent spots in plane Poiseuille flow. *J. Fluid Mech.* **178**, 405–421.

HENNINGSON, D. S., JOHANSSON, A. V. & ALFREDSSON, P. H. 1994 Turbulent spots in channel flows. *J. Engng Maths* **28**, 21–42.

LAGHA, M. & MANNEVILLE, P. 2007 Modeling of plane Couette flow. I. Large scale flow around turbulent spots. *Phys. Fluids* **19**, 094105.

LEMOULT, G., AIDER, J.-L. & WESFREID, J. E. 2013 Turbulent spots in a channel: large-scale flow and self-sustainability. *J. Fluid Mech.* **731**, R1.

LUNDBLADH, A. & JOHANSSON, A. V. 1991 Direct simulation of turbulent spots in plane Couette flow. *J. Fluid Mech.* **229**, 499–516.

MANNEVILLE, P. 2015 Towards a model of large scale dynamics in transitional wall-bounded flows, arXiv:1504.00664.

PHILIP, J. & MANNEVILLE, P. 2011 From temporal to spatiotemporal dynamics in transitional plane Couette flow. *Phys. Rev.* E **83**, 036308.

PRIGENT, A. & DAUCHOT, O. 2005 Transition to versus from turbulence in subcritical Couette flows. In *IUATM Symposium on Laminar–Turbulent Transition and Finite Amplitude Solutions*, pp. 195–219. Springer.

PRIGENT, A., GRÉGOIRE, G., CHATÉ, H., DAUCHOT, O. & VAN SAARLOOS, W. 2002 Large-scale finite-wavelength modulation within turbulent shear flows. *Phys. Rev. Lett.* **89**, 014501.

SCHUMACHER, J. & ECKHARDT, B. 2001 Evolution of turbulent spots in a parallel shear flow. *Phys. Rev.* E **63**, 046307.

TILLMARK, N. 1995 On the spreading mechanisms of a turbulent spot in plane Couette flow. *Eur. Phys. Lett.* **32**, 481–485.

TILLMARK, N. & ALFREDSSON, P. H. 1992 Experiments on transition in plane Couette flow. *J. Fluid Mech.* **235**, 89–102.

TUCKERMAN, L. S., BARKLEY, D. & DAUCHOT, O. 2008 Statistical analysis of the transition to turbulent–laminar banded patterns in plane Couette flow. *J. Phys.: Conf. Ser.* **137**, 012029.

TUCKERMAN, L. S., KREILOS, T., SCHROBSDORFF, H., SCHNEIDER, T. M. & GIBSON, J. F. 2014 Turbulent–laminar patterns in plane Poiseuille flow. *Phys. Fluids* **26**, 114103.

VAN ATTA, C. 1966 Exploratory measurements in spiral turbulence. *J. Fluid Mech.* **25**, 495–512.

https://doi.org/10.1017/jfm.2017.140 Published online by Cambridge University Press